

# Self-healing of drying shrinkage cracks in cement-based materials incorporating reactive MgO

T S Qureshi<sup>1\*</sup>, A Al-Tabbaa<sup>1</sup>

<sup>1</sup>Department of Engineering, University of Cambridge, Trumpington Road, Cambridge CB2 1PZ, UK

\*E-mail: tsq20@cam.ac.uk

**Abstract.** Excessive drying shrinkage is one of the major issues of concern for longevity and reduced strength performance of concrete structures. It can cause the formation of cracks in the concrete. This research aims to improve the autogenous self-healing capacity of traditional Portland cement (PC) systems, adding expansive minerals such as reactive magnesium oxide (MgO) in terms of drying shrinkage crack healing. Two different reactive grades (high “N50” and moderately high “92-200”) of MgO were added with PC. Cracks were induced in the samples with restraining end prisms through natural drying shrinkage over 28 days after casting. Samples were then cured under water for 28 and 56 days, and self-healing capacity was investigated in terms of mechanical strength recovery, crack sealing efficiency and improvement in durability. Finally, microstructures of the healing materials were investigated using FT-IR, XRD, and SEM-EDX. Overall N50 mixes show higher expansion and drying shrinkage compared to 92-200 mixes. Autogenous self-healing performance of the MgO containing samples were much higher compared to control (only PC) mixes. Cracks up to 500  $\mu\text{m}$  were sealed in most MgO containing samples after 28 days. In the microstructural investigations, highly expansive Mg-rich hydro-carbonate bridges were found along with traditional calcium-based, self-healing compounds (calcite, portlandite, calcium silicate hydrates and ettringite).

**Keywords.** Drying shrinkage crack, expansive minerals, strength recovery, crack sealing, durability improvement, healing materials microstructure.

## 1. Introduction

Drying shrinkage in cement-based materials is one of the major causes of mechanical strength reduction and crack formation. Shrinkage is developed during the progression of cement hydration process when moisture is lost from the specimen. Once a sample dries, a negative pressure develops inside the matrix pores due to lack of water required in the cement hydration process, thus resulting in a shrinkage stress. Shrinkage cracks typically initiate when the internal stresses developed in the cement-based matrix due to shrinkage stress are restrained. Moisture loss can further develop a moisture gradient across the hardened cement paste matrix, thus resulting in a differential shrinkage [1]. This causes formation of cracks due to self-restraining. Those cracks are formed perpendicular to the surface [2], [3] as the tensile stresses develop parallel to the drying surface and cracks start to form in early stages. Shiotani et al. [4] have reported that these early stages often start as early as 6 min on drying. Shrinkage cracks in cement-based systems also develop when external restraint is caused by the surrounding structure, such as the aggregates and reinforcements. Cracks due to this external restraint are typically radial and bond cracks form around the external higher stiffness substance [5] that caused the restraint. The widths of those cracks are larger than those of self-restrained types. However, stress associated with both self and external restraints in the cement-based matrix results in

the formation of drying shrinkage cracks, and they keep increasing with time. While drying in cement-based materials causes formation of drying shrinkages cracks, curing them back under water can stop this shrinkage and accelerate the hydration process. This re-hydration process in the matrix can initiate the formation of compounds, which can trigger the self-healing of the materials through crack healing and restoring its mechanical properties.

Self-healing in cement-based materials occurs due to hydration of un-hydrated cement remaining in the matrix. This is an intrinsic cement-healing property, which is termed as autogenic self-healing [6]. This phenomenon was spotted early in the mid-nineteenth century by [7] and the concept was gradually established by [8]–[12]. Early age concrete naturally heals rapidly due to autogenous self-healing [13], as it contains higher proportions of un-hydrated cement in the matrix. It was also established that fibres in the concrete improve autogenous self-healing [14]–[17] as they can restrict the crack width making it closer, thus triggering the self-healing mechanisms. Recently, researchers have been trying to improve the autogenous self-healing capacity with different kinds of expansive minerals additives [18]–[22], which have been found to be successful to some extent.

Autogenous self-healing of concrete in the actual environmental exposure condition was recently studied by several researchers. Self-healing of engineered cementitious composites (ECC) was studied by [23] in natural environment. They have reported self-healing recovery in the damaged ECC using resonant frequency, stiffness and first cracking strength recovery. Another study with the self-healing of ECC in the natural environment have further suggested that environmental conditions such as high rainfall rate facilitates this autogenous self-healing process [24]. Recently scientists of the University of Tokyo have repaired 85% of a 195 Km tunnel with their proposed self-healing cement materials and investigated their self-healing performance in natural environment [25]. Their repairing cement was PC-based systems with CSA-based expansive agent, geo-materials and chemical additive of the carbonate group. Their repair works results in a considerable recovery of those water leaks within 1-3 week and self-healing was found stable after one year. Besides advancement in the autogenous self-healing study for natural damage and recovery, bacterial-based autonomic self-healing was studied by [26] for outdoor environment applications. They have reported highly proficient calcification by bacterial-based concrete materials for efficient self-healing.

Moderately reactive grade MgO (92-200) was found to improve the autogenous self-healing capacity in our previous studies [18]. Following the success in the autogenous self-healing performance, M92-200 grade MgO was used in the concentric healing mineral glass capsule self-healing systems [27], where it again shows efficient self-healing performance. The reactive MgO is not only used for self-healing but also typically used for optimising the shrinkage performance of the concrete. While M92-200 is a moderately reactive grade of MgO used for different purposes, researchers have also used highly reactive grades of MgO to mitigate concrete's shrinkage performance [28]. Therefore, both of the reactive grades of MgO have a great potential to solve the drying shrinkage crack self-healing issue.

This research is aimed at improving the autogenous self-healing capacity of PC adding reactive MgO, in terms of drying shrinkage crack healing. Two different reactive grades of MgO (M92-200 and N50) were used to serve this purpose. Hence, a complete investigation was carried out in this study to characterise both MgO grades' influence over the drying shrinkage crack autogenous self-healing performance of PC.

## 2. Materials and experimental procedure

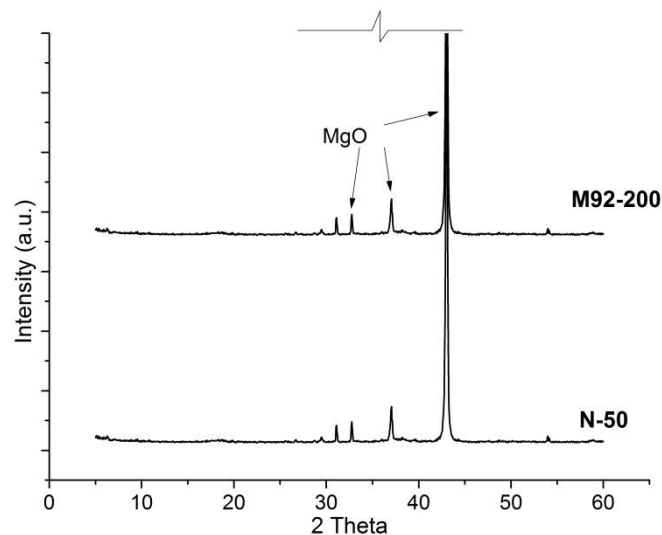
### 2.1. Materials and sample preparation

In this study, two different reactive grades of MgO in different proportions were used as expansive additives in PC. The PC was CEM I (52.5N) locally supplied by Hanson, UK, satisfying BS EN 197-1 [29] and has been selected as principal cement component. Typical clinker of PC is predominantly composed of mineral alite ( $3\text{CaO}\cdot\text{SiO}_2$ ), belite ( $2\text{CaO}\cdot\text{SiO}_2$ ), aluminat ( $3\text{CaO}\cdot\text{Al}_2\text{O}_3$ ), and ferrite ( $4\text{CaO}\cdot\text{Al}_2\text{O}_3\cdot\text{Fe}_2\text{O}_3$ ), all of which react with water and produce hydration products. Out of two reactive grade MgO minerals, one was M 92/200 a moderately reactive MgO produced from calcination of magnesite and the other was N50 a highly pure and reactive grade of MgO synthesized from sea water. Both types of MgO were supplied by Richard Baker Harrison Ltd, UK (source: China). The chemical composition and physical properties of PC and MgOs are listed in table 1.

**Table 1.** Chemical and Physical properties of PC and MgOs.

	PC: CEM I 52.5N	MgO (92-200)	MgO (N50)
<b>Chemical properties</b>			
SiO <sub>2</sub> (%)	19.50	2.25	--
Al <sub>2</sub> O <sub>3</sub> (%)	4.90	0.22	--
CaO(%)	63.60	0.87	0.50
Fe <sub>2</sub> O <sub>3</sub> (%)	3.10	0.53	0.03
MgO(%)	0.90	93.18	97.7
SO <sub>3</sub> (%)	3.30	--	0.80
Na <sub>2</sub> O(%)	--	--	--
K <sub>2</sub> O(%)	--	--	--
TiO <sub>2</sub>	--	--	--
CaCO <sub>3</sub>	--	--	--
LOI(%) -Loss on ignition	2.10	2.59	5.4
<b>Physical properties</b>			
Avg. Particle Size (µm)	5.00-30.00	30-40	15.06
Density (g/cm <sup>3</sup> )	2.75-3.20	3.02	3.59
S. Surface area (m <sup>2</sup> /g)	0.30-0.40	16-20	110.82
Reactivity (seconds)	--	145	11

Few physical properties of MgO in table 1 was collected from reference [30]. The chemical reactivity of MgO was measured using an accelerated reactivity test (as described in [31]) and a pH meter (integrated Wagtech International) was adjusted in the system (as described by [32]). The major differences between two MgOs were their reactivity, particle size and the contents of MgO. However, the X-ray diffraction (XRD) pattern of both minerals was similar (figure 1) except that N50 shows higher intensity in the major peaks for MgO around  $\sim 43$  ( $2\theta$ ) which may indicates its more purity.



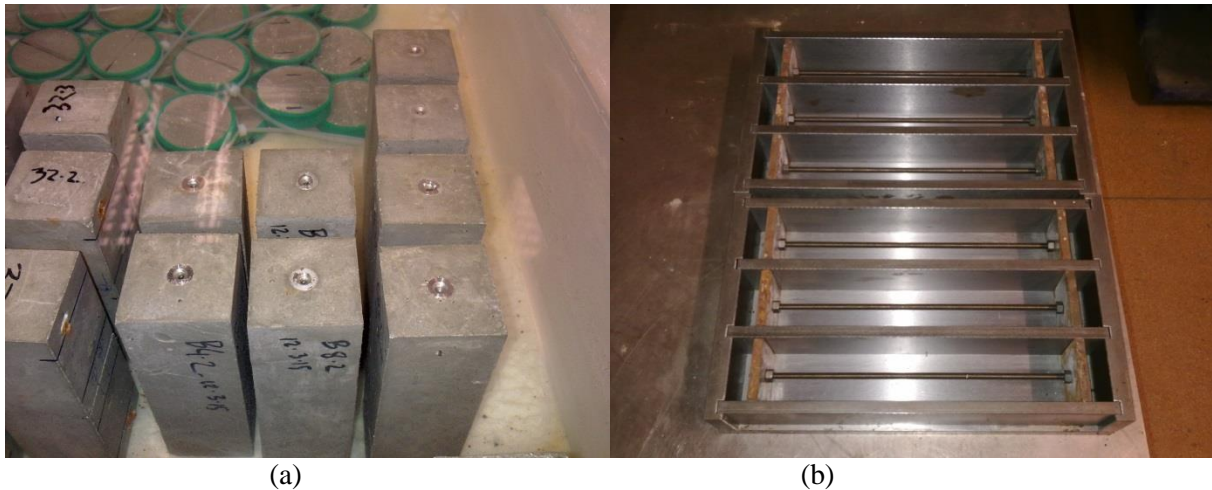
**Figure 1.** XRD of pure MgOs used in this experiment.

Table 2 illustrates the mix designs used in this study. Here the control mix (CON) is a typical cement paste mix, while the rest of the mixtures contain different percentages of MgO additives.

**Table 2.** Cement mixes with MgO additives by percentage weight.

Mixes	PC (%)	MgO	
		92-200	N50
CON (PC 100%)	100	-	-
M92-4	100	4	-
M92-8	100	8	-
M92-12	100	12	-
N50-4	100	-	4
N50-8	100	-	8
N50-12	100	-	12

The mixes were prepared in a rotating pan mixture of 20 Kg capacity and the moulds were filled in three layers. The water to cement ratio was kept at 0.35 for all mixes. Additives were mixed with PC in dry state then water was added in different sequence to prepare the cement paste. Pouring of each layer was followed by subsequent vibration using an electric motor vibration table. Cube samples (40mm x 40mm x 40 mm) were prepared for compressive strength analysis. Traditional shrinkage measuring prism samples (40mm x 40mm x 160mm) with end stud were prepared without reinforcement for shrinkage/expansion measurement as in figure 2a. Restraining end samples for drying shrinkage crack forming were prepared in the prism moulds (50X50X250 mm) with two end plates and a reinforcing bar in the middle (figure 2b). Finally discs of 50 mm width and 15 mm depth were prepared for gas permeability tests. Cast cylinders of 100 mm depth and 50 mm width were sliced into 15 mm thick disks using a trimmer saw and prepared for testing and full size cylinders were used for splitting tensile test.



**Figure 2.** Sample preparation and curing, a) prism samples (40mm x 40mm x 160mm) with end studs and b) restrained end prism moulds (50X50X250 mm) for drying shrinkage crack healing test.

All samples were left to set for 24 hr after casting and samples were demoulded afterwards. Required samples were then cured in ambient (RH ~60%) and immersed in water condition at  $\pm 20^{\circ}\text{C}$  in desirable periods for different experiments.

## 2.2 Experimental procedure

**2.2.1. Shrinkage test.** Shrinkage test was used to measure the shrinkage/expansion of different cement mix combination according to [33]. Triplicate prisms of 40X40X160 mm and 50X50X250 mm with restrained end samples were prepared and their shrinkage performance in ambient and immersed curing condition was monitored up to 28 days. The change of prism length was measured by a CONTROLS electronic length comparator having an accuracy of  $\pm 0.001$  mm. The initial sample length was measured immediately after demoulding. Further during the tests, the calibration rod length was measured between each mix set of prisms.

**2.2.2. Compressive and tensile strength test.** The 28 day compressive and tensile strength of hardened cement pastes in this study were obtained following BS EN 196-1 [34]. The tests were performed on the 40 mm cubes and cylinder (50 mm x 100mm) cement paste samples.

**2.2.3. Mechanical strength recovery due to self-healing.** Restraining end prism samples (50X50X250 mm) were left in the ambient condition for 28 days when natural drying shrinkage cracks started to form and extended over time. Cracks in the prisms appeared randomly however perpendicular to the drying surface and mechanical strength of the prisms reduces during this process. A three-point bending test was performed to measure the strength of the prisms before and after healing. Initially the strength performance of the cracked prisms was measured then they were cured under immersed in water condition for 28 and 56 days prior to testing their strength recovery performance. A typical three-point bend test setup is illustrated in figure 3. In the initial testing phase, prisms were expected to fail through the cracked path widening rather than formation of a new crack in the mid span zone. The effective span on that test was 200 mm and the loading rate was set at 0.125mm/min. First loading test on the shrinkage cracked samples was continued until a drop on loading was noticed due to crack widening which was mostly between the mid-span displacement in the range of 0.15-0.25 mm. Samples were little loaded prior starting the test to avoid low initial stiffness. Further correction was performed during data processing to correct any error in the initial load vs deflection data.

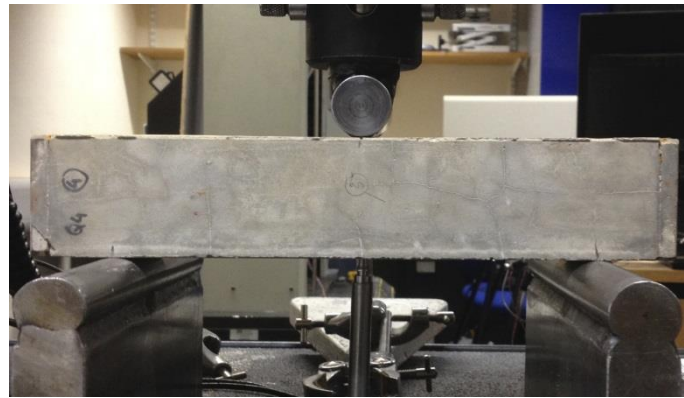


**Figure 3.** Three-point bend test setup in the restrained end prism samples.

The stiffness and cracking loads were expected to improve after self-healing from the initial loading to reloading stage. Hence the self-healing strength improvement was calculated using the first cracking load lapsing recovery ( $R_{load}$  %) and stiffness improvement ( $R_k$  %) using equations 1 and 2. Similar self-healing strength recovery evaluation formulae were also adopted by [23].

$$R_{load}(\%) = \frac{P_{rec}}{P_{ini}} \times 100\% \quad (1)$$

$$R_k(\%) = \frac{K_{rec}}{K_{ini}} \times 100\% \quad (2)$$

The calculation notations are illustrated in figure 4 using a typical loading and reloading curves. Where  $P_{ini}$  is the first cracking load and  $K_{ini}$  is the stiffness in the initial loading, and  $P_{rec}$  is the first cracking load and  $K_{rec}$  is the stiffness in the reloading after healing. According to these equations, both  $R_{load}$  (%) and  $R_k$  (%) have to be larger than 100% in case there is any self-healing occurs in prisms.

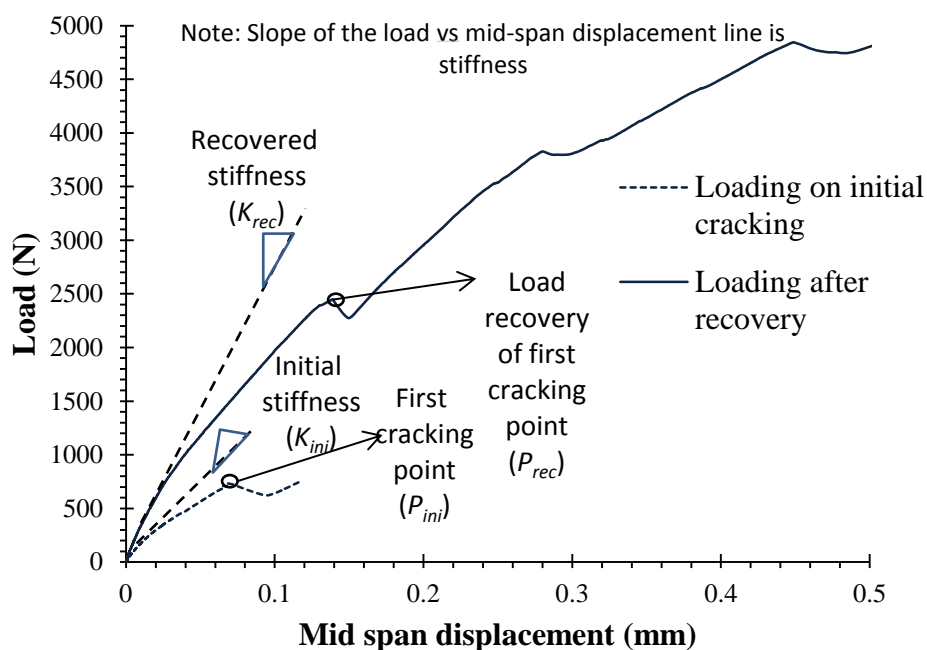


**Figure 4.** Terminologies in a typical load vs displacement graph of restrained end prisms.

However the endplate connecting with a centroidal bar systems in the restraining end prisms had played an important role by reinforcing the samples during entire experiment. Firstly the bar was acting like restraints assisting in the shrinkage crack formation and it was holding up segments of hardened samples throughout the natural drying shrinkage cracking stages. Secondly it makes the three-point bending test in the damaged prisms before and after healing stable by producing comparable measurements avoiding random failure. Finally the bar systems had restrained the samples at the end while they were expanding for curing under water. Restraining the expansion of the cement had allowed cracks to come in closer which had triggered the self-healing process.

*2.2.4. Crack sealing performance measurement.* Cracked prisms after initial three-point bending were marked in different spots across the crack randomly. Images were taken on the marked spots using a GXCAM 1.3 type digital stereo microscope over recovery periods. Image analysis software (Image-J) was then used to analyse the acquired captions, crack width and the total crack area for each case. The crack-sealing efficiency was evaluated by the percentage of the crack area closure over time, CA (%) using following equation:

$$CA(\%) = \frac{CA_0 - CA_t}{CA_0} \times 100 \quad (3)$$

where  $CA_0$  is the crack cross-section area just after cracking and  $CA_t$  is the crack cross-section area after healing time  $t$ .

*2.2.5. Self-healing materials microstructure investigation.* Micro-structure of the self-healing materials were studied using X-Ray diffraction (XRD), Fourier transformed infrared spectroscopy (FT-IR) and Scanning Electron Microscopic (SEM) imaging with Energy Dispersive X-Ray (EDX) analysis. The samples were collected from healed surface following the final loading tests on the restrained end prism samples. The sample collection, preparation and testing was performed as similarly described in [35], [36].

*2.2.6. Capillary water absorption test as durability indicators.* A short-term one-dimensional sorptivity test as described in the technical guidelines by RILEM [37] was used to measure one of the durability performance of self-healing. Water absorption test was performed on the restrained end prisms initially after the three-point bend test, and a second time after healing for 28 days in immersed condition. The prism side which was downward in the three-point bend test, was set in the water surface to perform the test as shrinkage cracks were appeared in the sample randomly and cracks on that side were widen mostly during loading. The exact same side of the healed samples was set in the water surface second time. Samples were dry in the first water absorption test. However during the second test series, samples were placed in the oven at 40°C for 72 hours to remove moisture after they were cured in the water for 28 days. Samples were dried prior testing and all samples weight losses were less than 0.5 gm between final 24 hr of drying. Weight changes of the specimens due to capillary suction were monitored for ~4.5 hours in all specimens. The sorptivity coefficient was measured using following formula according to [38]:

$$M_w = S\sqrt{t} \quad (4)$$

where  $M_w$  is the water suction quantity per unit area and  $S$  is the sorptivity coefficient of the cement-based systems, regressed as the slope of the curve between  $M_w$  and the square root of time  $t$ .

*2.2.7. Coefficient of gas permeability measurement as durability indicators.* This is another durability indicators used to evaluate the self-healing performance. The coefficient of gas permeability was

evaluated using liquid methanol as the gas source following [39]. All disc samples after 28 days curing in ambient conditions were cracked using the same INSTRON 30 KN loading cell with the loading rate of 0.125 mm/min and allowing a crack opening up to ~0.50 mm. Then samples were cured under water for another 28 days and then dried under vacuum for 48 h at 20 ~°C room temperature to remove moisture. Like the sorptivity test samples, the weight losses in the discs were less than 0.5 gm in in final 24 hr prior testing. The rest of the sample preparation and testing process was similar as described in [35]. The gas permeability coefficient (k) was measured from the steady-state mass loss over time in the 40°C water bath using following equations [40]:

$$k = \alpha \frac{L}{A} m^* \quad (5)$$

$$\alpha = 2\eta T R_u \frac{P_2}{(P_1^2 - P_2^2)} \quad (6)$$

where L= the length of the sample (m), A = the cross-sectional area perpendicular to the direction of flow (m<sup>2</sup>), m\* = the rate of mass loss (g/hr), and  $\alpha$  is a constant for methanol in a particular temperature and pressure difference, calculated from  $\eta$  = the dynamic viscosity (Ns/m<sup>2</sup>), T= the absolute temperature (K),  $R_u$  = molecular weight x the universal constant (8.3 J/mol K, for methanol,  $P_1$  = the inlet pressure (N/m<sup>2</sup>), and  $P_2$  = the outlet pressure (N/m<sup>2</sup>).

### 3. Result and discussion

#### 3.1. Shrinkage performance of different mixes

Figure 5 shows the shrinkage and expansion measurement results using prisms (40x40x160 mm) with end stud. In the graph, time 'zero' was the initial sample length measurement day after demoulding the samples at one day i.e. 24 hr after casting. Following demoulding and taking the first length measurements, samples that were left in laboratory ambient environment (~20°C and 60% RH) undergoes shrinkage and samples cured in the water undergoes expansion over time. As discussed in the literature of introduction section, this was due to the development of pores in the cement matrix during the cement hydration process. Initially, these pores fill with the extra water in the matrix and the pore water was used in the continuation of hydration process. While this pore water was evaporated and used in the cement hydration process, a negative pressure developed inside the pores, which caused shrinkage in the hardened cement matrix. This process triggered when the cement end stud prism samples were left in an ambient condition due to the evaporative water loss from the matrix causing drying shrinkage. In contrast, cement samples that were cured under immersed in water condition keep expanding due to continuation of hydration. As the continuation of the hydration results in a continuous formation of hydrated products which densify cement matrix attributes in an ultimate expansion.



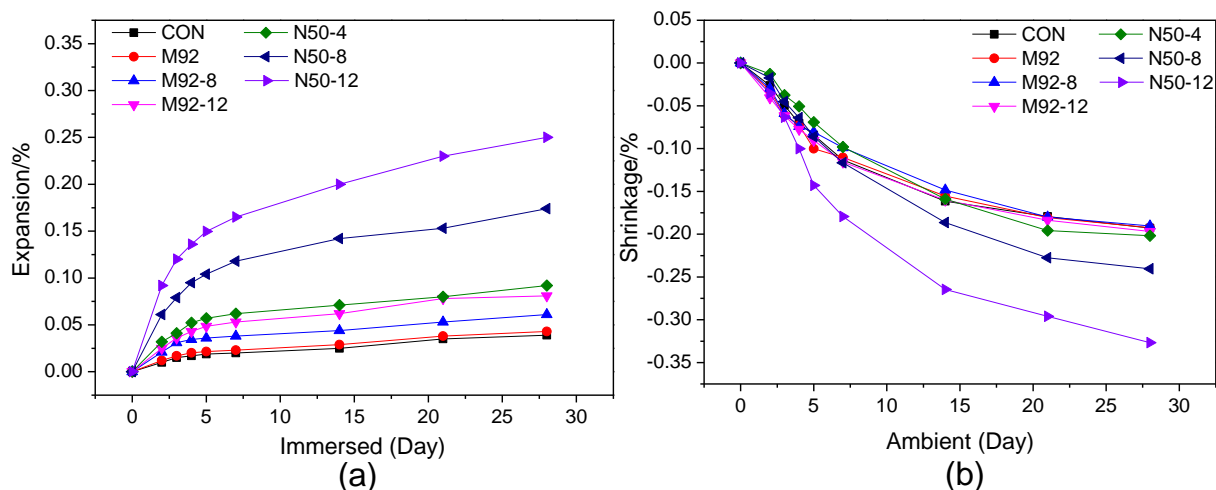


**Figure 5.** Change in length percentage with MgO mineral additives: (a) Expansion for curing in water immersed condition, and (b) Shrinkage for curing in ambient condition.

The hydration process along the first five days plays a very important role in the shrinkage and expansion behaviour (figure 5). Higher proportions of both types of MgO addition show greater shrinkage and expansion effects. Here, N50-containing samples show higher shrinkage and expansion compared to M92-200 samples. The shrinkage of M92-200 mixes in ambient condition were similar or a little lower compared to control, while the expansion in the immersed condition showed an increase of 1.5-2 times for 8 to 12% of MgO in 28 days. However, this was not the same case for MgO-N50 mixes, as additions of 8 to 12% have resulted in an increase of about 1.25-1.75 times in ambient shrinkage, and a 4.46-6.41 times increase in expansion in the immersed condition compared to control samples. This was due to the faster hydration reactivity property of N50 compared to M92-200. The microstructure of the MgO, its particle size and specific surface area played an important role in its hydration and expansion behaviour. The smaller particle size of MgO-N50 has a comparatively larger specific surface area, thus resulting in a larger reaction interface with water for hydration. This leads to a faster hydration rate and corresponding faster and larger expansion at early age. Similar findings were reported by [30], [41]. Considering these results, it could be noted that about 4-8% MgO (M92-200) have resulted in the least drying shrinkage and considerable expansion in immersed conditions, whereas N50 samples showed much larger shrinkage and expansion. The N50-12 mixes were avoided in the next stages of the experiments, as this shows extremely larger shrinkage and expansion behaviour, which was regarded as not feasible for practical application.

### 3.2. Compressive and tensile strength development

The compressive and tensile strength development over 28 days is shown in figure 7. Higher proportions of MgO addition with PC have typically decreased the compressive strength, although an exception was found for 4% of M92-200 mixes, which results in a rather small increase in the strength compared to control samples. This indicates that the optimum compatibility of MgO (92-200) grades for compressive strength development lies between 4 to 8%, which was similarly found in our previous studies [18]. The compressive strength development of N50 mixes were always lower than 92-200 mixes, with N50-12 samples probably shows the least performance. These have indicated the negative effects in PC strength development due to the addition of excessive proportions of highly reactive MgO. The addition of expansive minerals also showed similar impact in the corresponding splitting tensile strength development of specimens at 28 days.

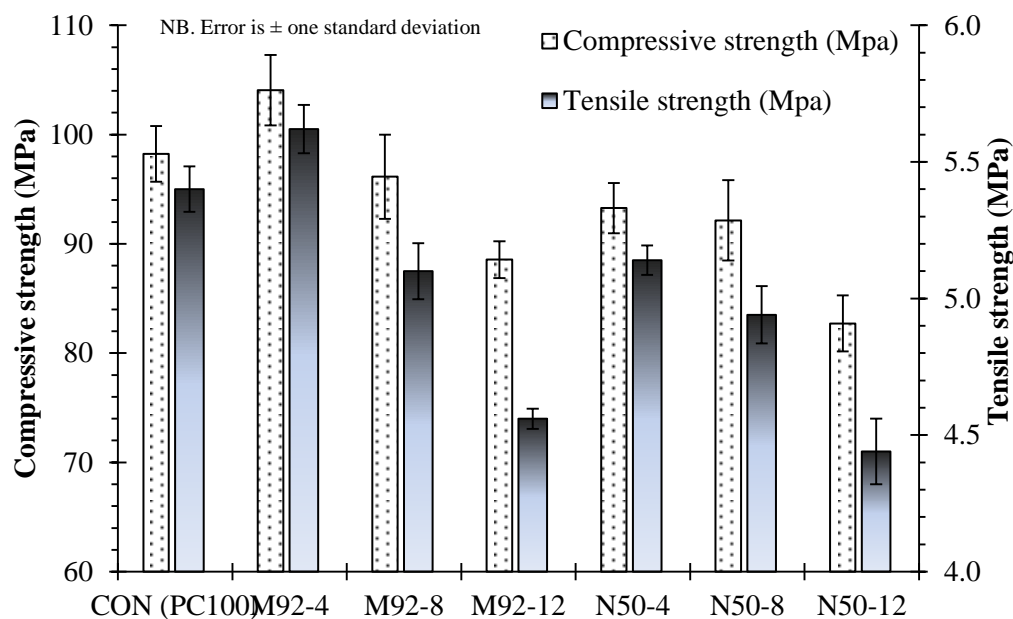


**Figure 6.** Compressive and tensile strength development with different cement mixes.

The hydration of MgO is triggered with the  $\text{OH}^-$  reactions with  $\text{Mg}^+$  from its boundary surface forming  $\text{Mg}(\text{OH})_2$ . An expansion model of MgO by [42] suggests that hydration in the high reactive MgO occurs on the exterior surface, inner pore surface, and the grain boundary forming localized  $\text{Mg}(\text{OH})_2$  near MgO contributing to the self-expansion of MgO particle in the pre occupied confined region. This expansion in the confined region produces expansive stress and eventually expands the cement matrix. On the contrary, less reactive MgO has less inner pores resulting less  $\text{Mg}(\text{OH})_2$  production and expansion in early stage, then ultimately larger expansion in later stage.

The expansion of MgO in the early stages of hydration results in a development of internal stresses inside the cement matrix. This is commonly known to be the reason for balancing the shrinkage stress in the cement. Optimum proportions of MgO in PC results in a compatible expansion through the partial MgO hydration by densifying the microstructure. In addition [32] suggests that the unconsumed MgO act as a filler materials to the micro-structure resulting in a further compacted matrix and ultimate increase in the strength properties. This kind of strength improvement was found in our samples with M92-4 which shows little increment in the compressive and tensile strength compared to control samples.

However addition of excessive proportions of reactive MgO than optimum limit can cause excessive expansion in early stages of hydration producing relatively more hydration products compared to the surrounding cement matrix. These may damage the PC-MgO hydration products interface resulting in an ultimate reduction in the strength development. In addition, MgO early age expansion has a relation to its reactivity and particle size as such, smaller the particle size, higher the MgO reactivity and faster the early age expansion. Hence optimum mix proportionate limit of M92 addition with PC was found higher than that of N50. This explains the reason for M92-4 samples higher strength development compare to N50-4 samples. Also the reductions of strength in higher proportions of MgO mixes compared to control samples.

In closing this section, it could be noted that MgO in the PC should be added in optimum proportions, considering their reactivity and expansive properties desired for improving other functionalities, such as thermal and shrinkage effect reduction and improving the autogenous self-healing capacity.

### 3.3. Mechanical strength improvement due to self-healing

The results of strength improvement due to autogenous self-healing in terms of first cracking load recovery and stiffness improvement are shown in figure 7. According to the equations 1 and 2, both  $R_{load}$  (%) and  $R_k$  (%) have to be greater than 100% in case there is any self-healing. The three-point bend test on restraining end prism samples before and after self-healing in this study showed improvements in both load recovery and stiffness for all samples. All MgO samples resulted greater recovery than control (figure 7(a)). MgO (M92-200) addition in prisms showed an increasing load recovery trend from 4 to 8%, then the recovery decrease for addition of 12%. Furthermore the all M92 mixes load recovery showed an increasing trend from 28 to 56 days. Overall N50 samples obtained lower load recovery compared to M92 samples. Although N50-8 shows higher load recovery compared to N50-4 at 28 days, this alters at 56 days. Therefore higher proportions of reactive MgO may have resulted in higher expansion in the cement matrix, which did not necessarily attributed in better recovery. There was a threshold of reactive MgO addition for obtaining optimum load recovery performance. This optimum range of MgO addition for M92 was around 8%, and for N50 it was between 4 to 8%.

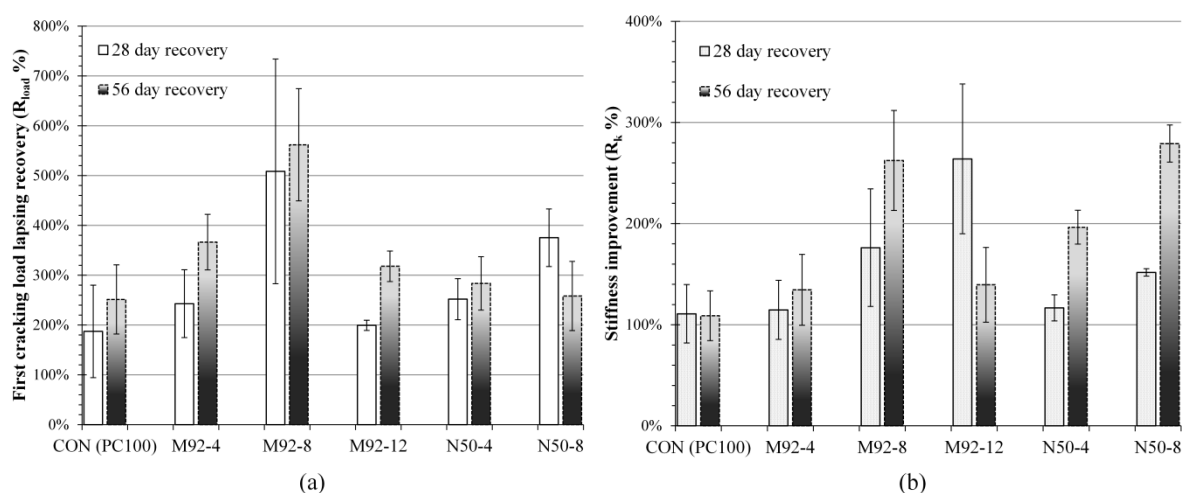


**Figure 7.** Strength improvement due to autogenous self-healing in 28 days and 56 days: (a) First load lapsing capacity improvement, and (b) Stiffness improvement.

The stiffness of the damaged prisms would have been substantially lower without the self-healing effect, as similarly reported by [15]. Stiffness improvements were found increasing with the addition of higher proportions of both types of MgO, where N50 shows a little stiffer compared to corresponding M92 samples (figure 7(b)). There was an improving trend from 28 days to 56 days stiffness with the exception of the M92-12 mixes. This discrepancy may be attributed to the wider crack range and higher stiffness in the initial loading stage prior self-healing, due to greater proportions of MgO. Overall expansive MgOs were expanding in the crack zone and cement matrix through a re-hydration process, which makes the samples stiffer over the curing time. Hence in most cases, higher proportions of expansive agents result in better stiffness recovery over time. This kind of recovery in stiffness could also attribute to the increase in cement based materials strength and modulus elasticity of the uncracked sections.

### 3.4. Crack sealing efficiency

Cracks in the restraining end prisms appeared due to the drying shrinkage. When cement matrix starts shrinking, the developed internal stress causes cracking around the surface and perpendicular to the centroidal restraining reinforcement bar. Typical visual crack sealing investigation over time is presented in figure 8. In each mix combination, crystalline superficial crack sealing materials started accumulating since the first day of curing under water. These were presumably carbonate crystals, typically calcite and some other carbonates, incorporating magnesium, aluminium and silicon ions.

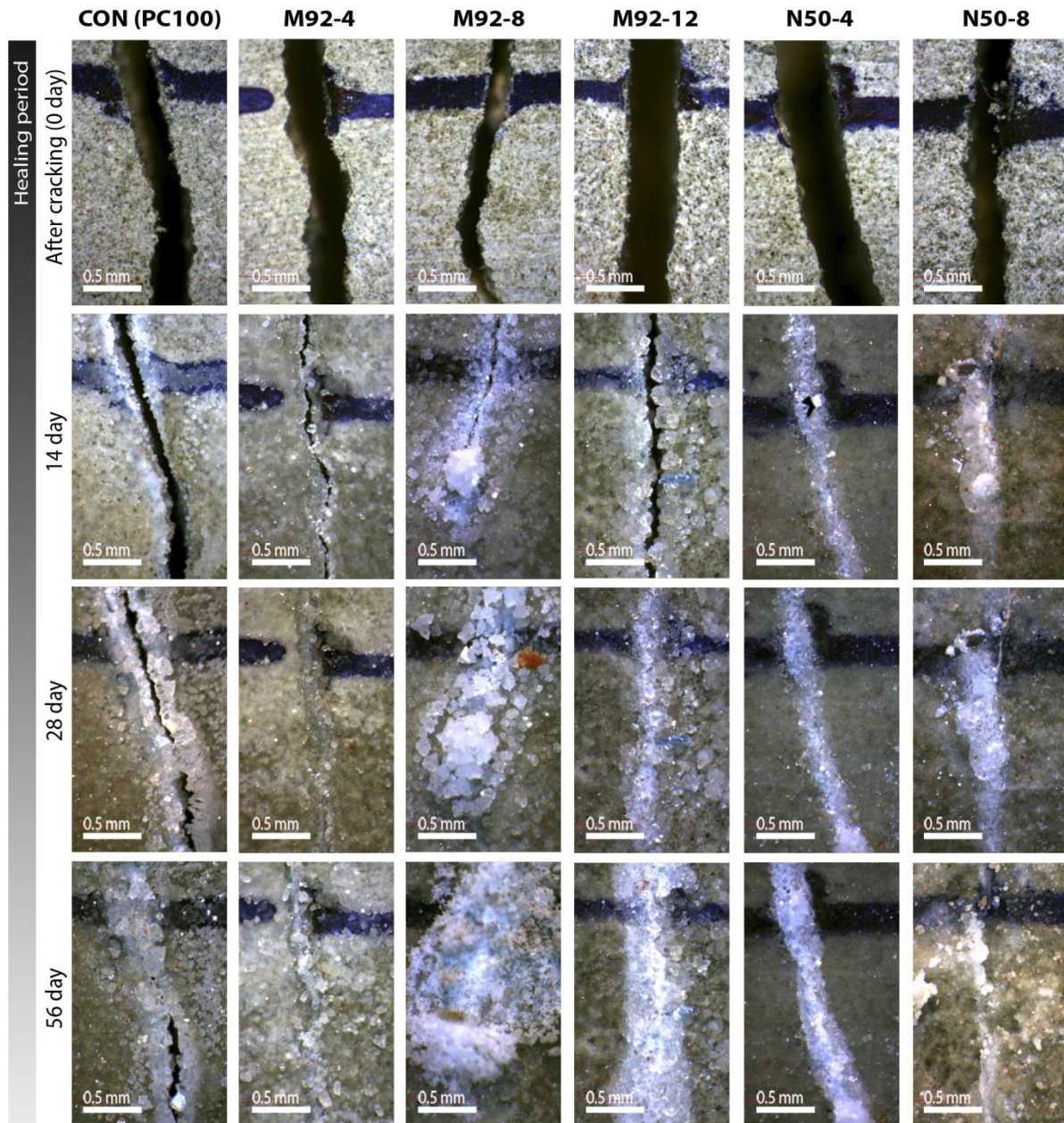


**Figure 8.** Typical crack sealing pattern of different mixes over time.

Cracks in MgO samples sealed faster compared to control. The N50 samples cracks were mostly sealed within 14 days, whereas it took about 14 to 28 days for M92 samples. Therefore, higher reactivity and proportions of MgO result in faster sealing performance. In addition, the expansive nature of the mixes has a positive effect on the crack sealing mechanisms in terms of reduction of the

crack width over time. This could be clearly noted from typical M92-12 and N50-4 wider cracks (figure 8), where the crack tips comes closer due to expansion of the matrix, which accelerates the sealing mechanisms.

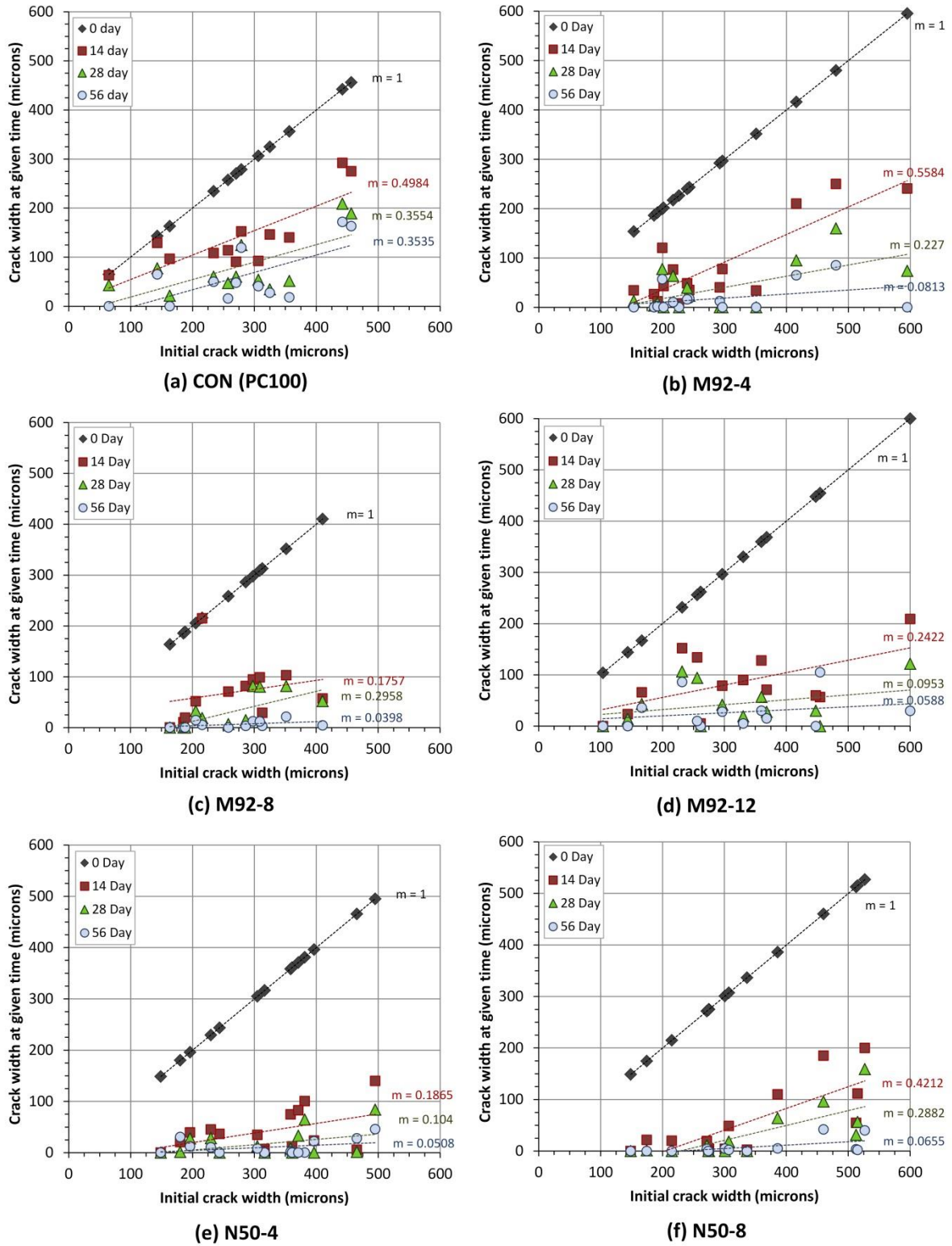
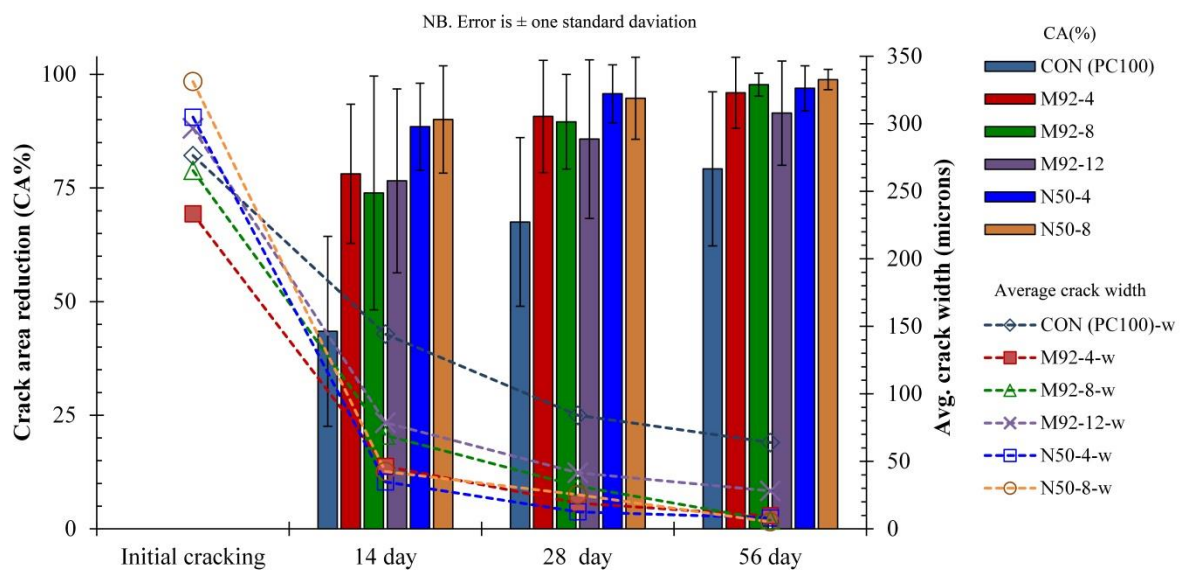


Figure 9. Initial crack width against the crack width reduction over time.

As the crack widths were randomly marked and monitored over the healing period, the crack width at a given time against the initial crack width results were plotted in figure 9. Smaller cracks were healing faster in all cases and cracks up to  $\sim 450 \mu\text{m}$  were found healed within the first 14 days in some MgO samples. A good majority of the wider range cracks in the MgO samples were closed much faster compared to the control samples, where the N50 samples show the most promising performance at an early age. Cracks up to  $160 \mu\text{m}$  were closing within 28 and 56 days for control samples, whereas the majority of cracks up to the range of  $400\text{-}500 \mu\text{m}$  were found sealed in MgO-samples. Crack width with time against initial crack width curves gradient (m) lowering was indicating trends of faster and wider range crack healing aptitude. This gradient reduction turns out to be quite promising for N50 samples, followed by samples containing higher proportions of M92 and least for control samples. Therefore, the reactivity of MgO and its higher mix proportions have increased the sealing rate and capacity of closing wider range cracks.



**Figure 10.** Crack area reduction percentage and average crack width over curing time.

Figure 10 shows the crack area reduction percentage and average crack width over time. Overall MgO samples results in a crack area reduction of about 74-99% between 14 to 56 days, which is much higher compared to the control samples 43-79% reduction in the same period. The rapid reactivity of N50-MgO results in about 88-90% crack sealing in 14 days, which was much higher than the M92 samples (74~78%) and control samples ( $\sim 43\%$ ). Although the M92 samples crack area reduction percentages were lower in 14 days, the reduction percentage increased up to  $\sim 90\%$  in 28 days and up to  $\sim 98\%$  in 56 days. This result is correlating with the corresponding samples MgO proportions and their associated reactivity, where N50 (11 s) was more reactive compared to M92 (145 s). It also agrees with Mo et al.'s [41] expansion model, as highly reactive MgO shows larger expansion at an early age, whereas a comparatively lower reactive MgO shows a lower expansion early, but nonetheless an ultimately larger expansion over time.

Average cracks width prior to healing was showing a trend of  $\text{M92-4} < \text{M92-8} < \text{CON} < \text{M92-12} < \text{N50-4} < \text{N50-8}$ , which was almost proportional to their drying shrinkage properties. This was as such, the greater the shrinkage, the larger the crack width. The higher proportions of reactive MgO (M92-12, N50-4 and N50-8) have resulted in wider shrinkage cracks in the prisms. Even the average crack widths were higher for N50 mixes, their crack sealing was most promising. As over 95% crack area reduction in N50 mixes was found at 28 days, and this showed a further improvement in 56 days

recovery. This was found not to be the case for M92-12 samples. In fact, the overall crack area reduction performances for M92 samples stands as  $M92-8 \geq M92-4 > M92-12$ , and both M92-4 and M92-8 reach a N50 samples area reduction percentage over 56 days, i.e., an almost complete crack sealing state. This could be due to M92-12 samples considerably wider shrinkage cracks prior initiating self-healing.

### 3.5. Microstructure characterisation of the formed healing materials

This section presents the self-healing materials microstructure characterisation based on FT-IR, XRD and SEM-EDX. The FT-IR spectra analysis graph is presented in figure 11, where similar infrared bands were observed regardless of different sample types. Characteristic H-O-H bond stretching was noted around  $3620 \text{ cm}^{-1}$  followed by shallow wide transmittances, which indicated the presence of portlandite:  $\text{Ca}(\text{OH})_2$  and brucite:  $\text{Mg}(\text{OH})_2$ . Following that, sharp bands around  $1424\text{-}1430 \text{ cm}^{-1}$  and  $870 \text{ cm}^{-1}$  confirmed the presence of carbonate phases ( $-\text{CO}_3^{2-}$ ) in all samples, which were similar to the findings of [43], [44]. The indication of ettringite presence was confirmed by the sulfate ( $-\text{SO}_4^{2-}$ ) stretching vibrations around  $1116$  and  $1118 \text{ cm}^{-1}$ . Similar findings were reported by [45], [46]. The deep banding around  $980 \text{ cm}^{-1}$  indicates the Si-O bonding for possible C-S-H presence. Researchers [45], [47] have further suggested that bending at  $530 \text{ cm}^{-1}$  could be an indication of magnesium incorporation in the C-S-H, as is evident in this case, although there was lots of noise effect in the signal for low range web numbers.

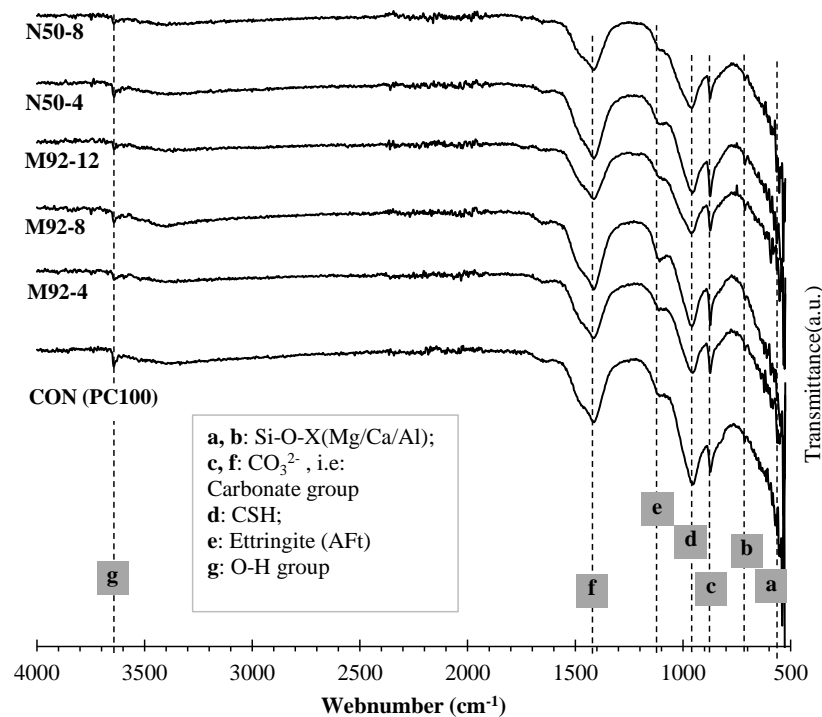


**Figure 11.** FT-IR analysis on the self-healing materials.

While FT-IR results identified basic self-healing materials, the influence of MgO in the healing compound formation was not possible to distinguish. This microstructure investigation has been taken forward with the XRD analysis on healing materials, as presented in figure 12. The presence of hydrated products such as portlandite, brucite, ettringite, C-S-H and carbonated calcite was confirmed again with characteristic XRD peaks. The influence of MgO in the healing compound formation was confirmed with the apparent strongest intensity for the major brucite peak at  $\sim 18.5^\circ$  and subsequent peaks for different phases of hydrous magnesium carbonate, such as dypengite, nesquehonite and

hydromagnesite. Further, hydrotalcite-type phases like  $(Mg_6Al_2CO_3(OH)_{16} \cdot 4H_2O)$  and calcium magnesium aluminate hydrate  $((C,M)_4AH_{13})$  may exist in the compound, as some of the peaks  $\sim (11.5^\circ, 23^\circ, 34.5^\circ$  and  $39^\circ)$  agree with similar observations reported in [48], [49]. Among other magnesium products, magnesian calcite peaks are similar to calcite peaks, thus making them difficult to distinguish.

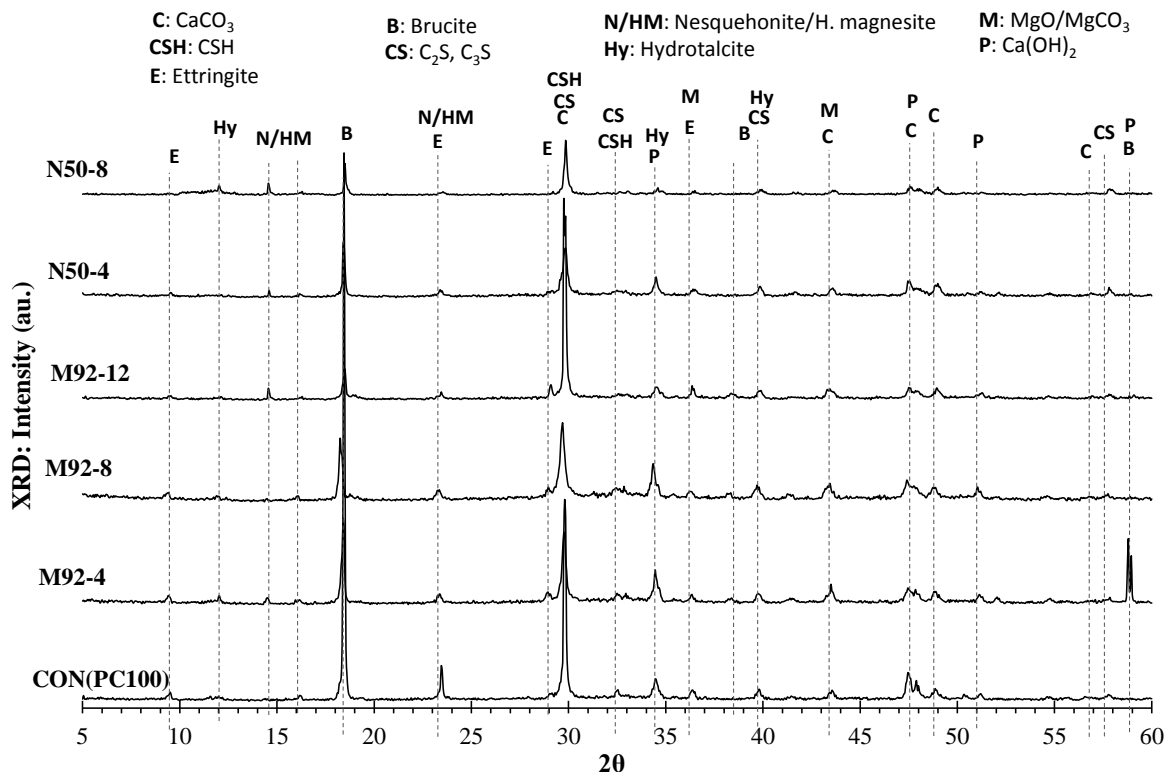
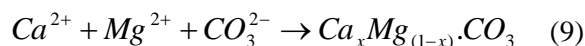
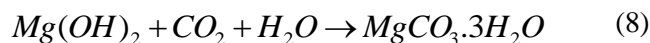


**Figure 12.** XRD analysis on the self-healing materials.

While ettringite peaks were dominant in the control healing samples, it was not the same in others. Magnesium oxide, on the other hand, has influence on the formation of additional hydration products, and this was evident with the increment on the peak intensity for Mg-rich products. Additional hydrated products increase the autogenous self-healing mechanism. The XRD overlapping intensities and FT-IR observations indicate the apparent complexity of the self-healing products formation due to MgO addition with PC. Different proportions and MgO type's addition influence will be further explained through the self-healing materials surface SEM imaging and EDX quantification results.

Typical microstructural surface morphology of self-healing materials is presented in figure 13. While control samples with only PC results in mostly Ca-rich products in the self-healing surface, such as calcite, portlandite and CSH (figure 13(a)), MgO in the other samples results in the considerable formation of Mg-rich products such as brucite, nesquehonite/dypengite/hydromagnesite and Mg-rich calcite (figure 13b-f). These can be as a result of the following reactions:





However, the hydro-carbonates of magnesium can co-exist in different phases [50] following the transformation trend below:

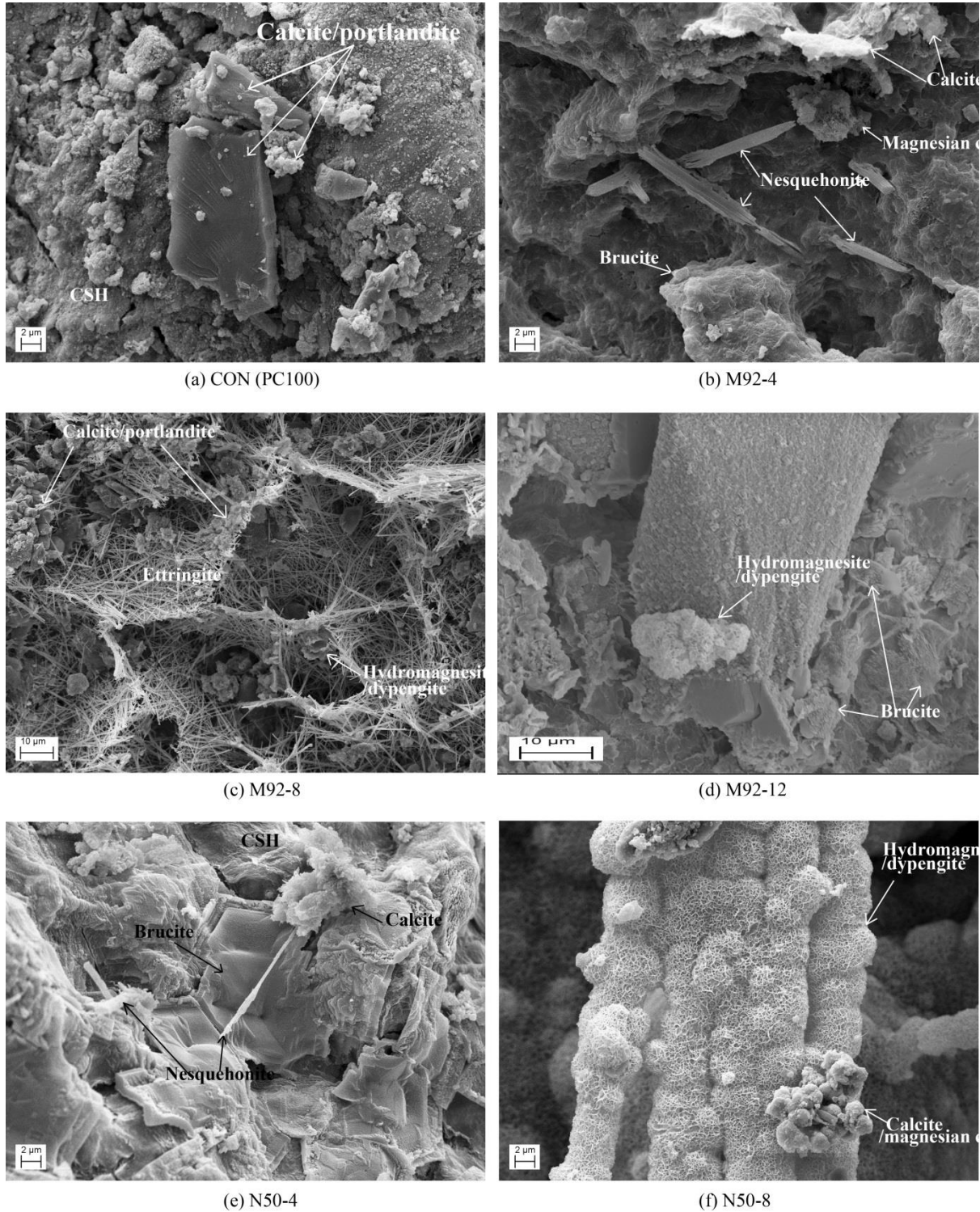
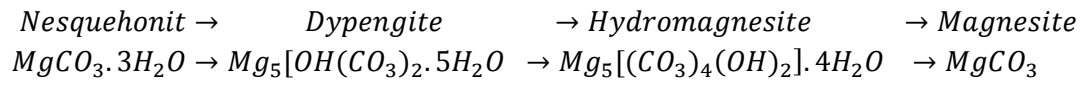


**Figure 13.** Typical microstructural morphology of the self-healing materials under SEM for EDX investigation.

The SEM images exhibit nesquehonite with pitted and irregular sub-spherical magnesian calcite crystals, and characteristic flower-like dypengite or hydromagnesite, similar to [51]. While nesquehonite and dypengite were found frequently in M92-4 to 8 and N50-4 healing compounds, hydromagnesite phases were common in M92-12 and N50-8. Hence, the higher proportions and reactivity of MgO shows a tendency to the formation of a more stable state of Mg-hydro carbonates.

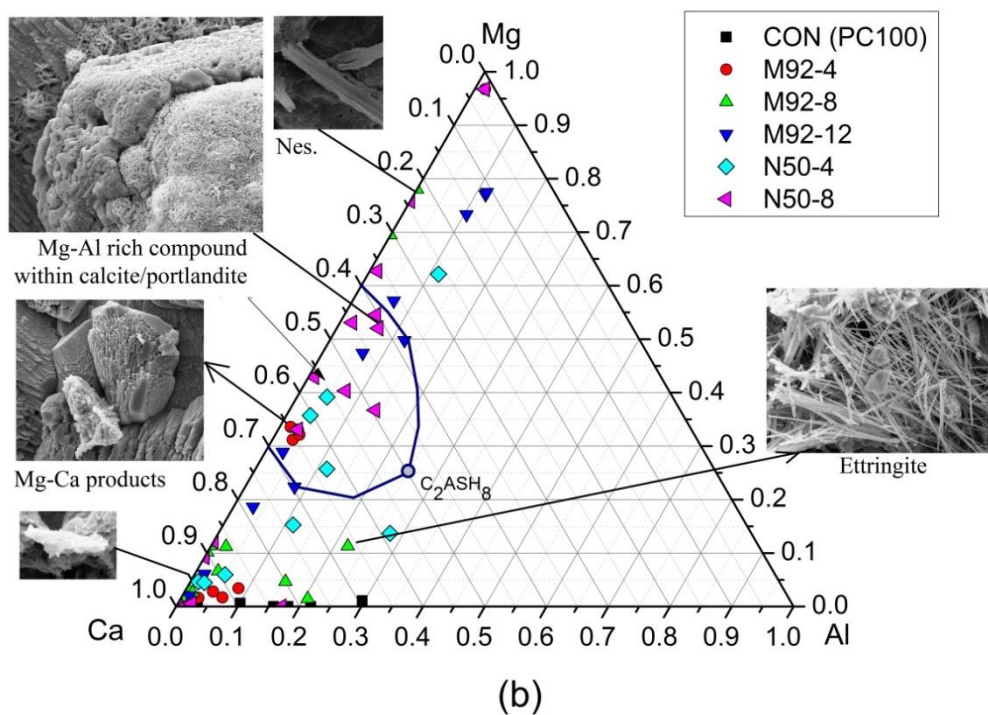
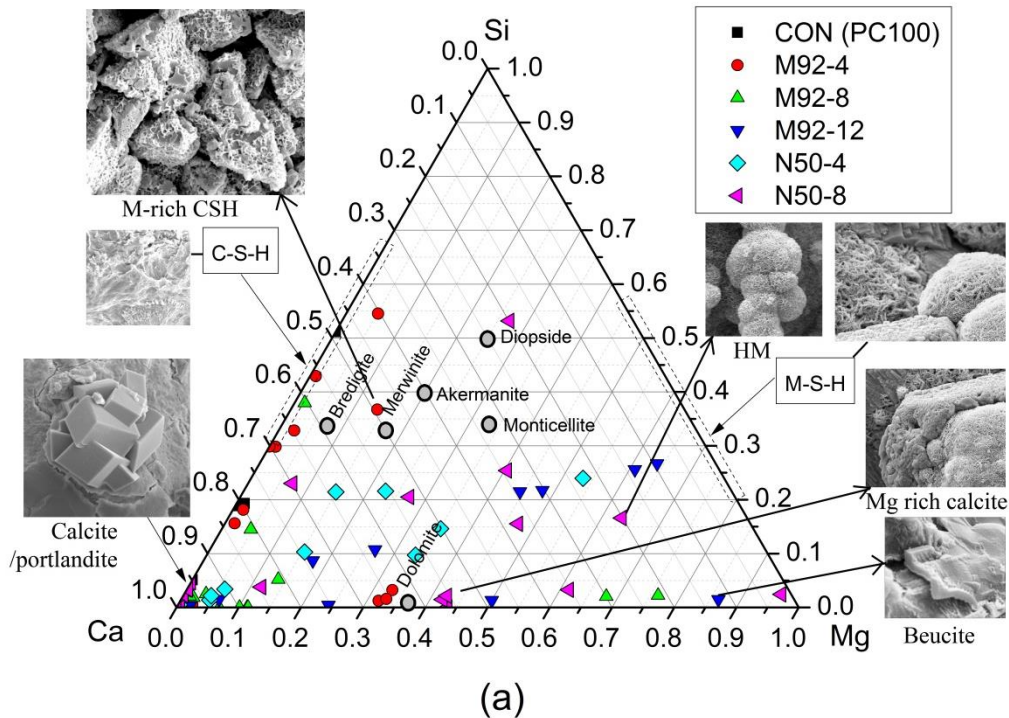


**Figure 14.** Atomic mass percentage correlations in ternary diagrams: (a) Ca-Mg-Si and (b) Ca-Al-Mg.

EDX elemental detection was carried out on several spots to quantify associated healing compounds elemental compositions. Self-healing materials elemental compositions was analysed using two ternary diagrams, Ca-Mg-Si and Ca-Al-Mg (figure 14). In the ternary diagrams, the normalised values of elements were taken from the atomic mass percentage of EDX detection and some typical SEM images of those detected spots were also attached. Few known Mg-rich minerals were plotted in figure 14(a), a ternary following the literature in [45], which suggests that the healing products compositions were close to some of those. Initially, the re-hydration process was triggered with the nucleation of un-hydrated cement and the growth of hydrated products. This hydration keeps continuing as long as un-hydrated cement remains in the matrix and water is available for the entire process. Let alone calcite and portlandite, the self-healing product analyses showed average composition ratios of Si/Ca  $\approx$  0.71, Al/Ca  $\approx$  0.11, Si/Mg  $\approx$  0.28, and Al/Mg  $\approx$  0.1. Here, Si/Ca was a little higher compared to common PC hydrated products recommending the value around 0.5 [52], as  $\text{Ca}^{2+}$  ions can more actively participate in the secondary hydration of the cement for self-healing. Hence, the self-healing products' density and strength was much lower than most of the cement hydrates in the initial cement mixing. Addition of MgO in the cement improves its expansion property in the re-hydration stage, which is important for autogenous self-healing. This now can be clearly seen in the ternary diagrams, that higher proportions and reactive grade MgO increase the Mg-based hydration product formation. This along with the Ca-based rehydration products from PC have resulted in a higher efficiency in the self-healing performance. The re-hydration process of the MgO-cements may effectively hydrate MgO, resulting in  $\text{Mg}^{2+}$  ions and endorsing, not only with hydrocarbonates but also in the calcite nuclei, aluminate and silicate hydrates. This was triggering more self-healing materials formation thus contributing into the densification of re-hydration products, which ultimately have improved the durability of the self-healing process.

### 3.6. Durability recovery indicators

Figure 15 shows the measured sorptivity coefficients for all samples after damaging with drying shrinkage crack formation for 28 days and subsequent healing for another 28 days. There were remarkable decreases in the water absorption in all samples before and after healing. The corresponding samples' sorptivity coefficient decrease was about 5 to 8 times after self-healing. This was because of the fact that cement matrix have densified with the continuation of hydration and the efficient self-healing of the formed drying shrinkage cracks. Without self-healing this would not be the case.

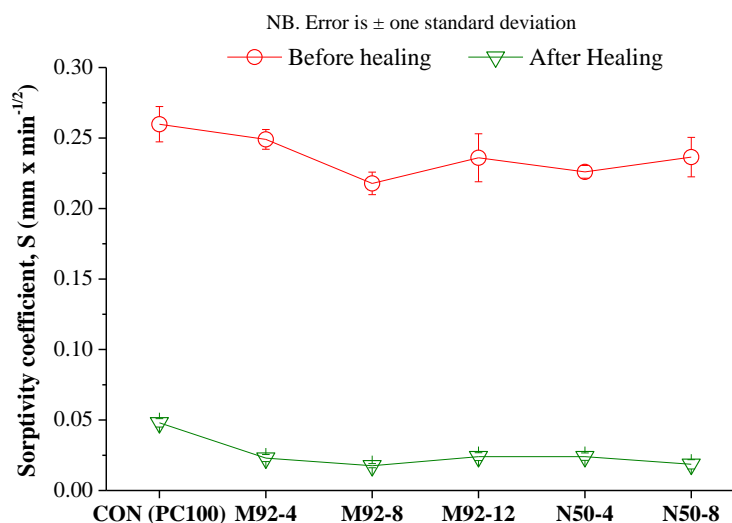


**Figure 15.** Improvement in the sorptivity coefficient before and after self-healing.

However, MgO addition has resulted in better improvement in terms of sorptivity coefficient reduction compared to control samples. The overall trend of the coefficient was  $M92-8 \leq N50-8 < N50-4 \leq M92-4 < M92-12 < \text{Control}$ . Therefore, higher proportions of MgO typically yield better performance.



**Figure 16.** Typical water absorption performance before and after healing (at 2 hr water absorption).

The sorptivity results have suggested that reactive MgO have effectively transformed the prisms, making them more watertight, through the formation of expansive hydrated products. The rehydration products' formations were described in the previous section. A typical comparison of the water absorption properties before and after healing is illustrated in figure 16. This image suggests that effective crack sealing has reduced the water absorption rate, which eventually resulted in a decrease in the sorptivity coefficient.

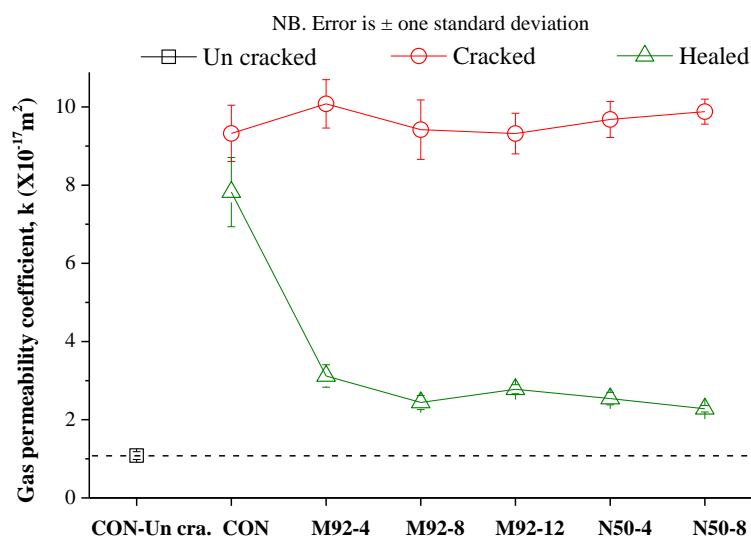


**Figure 17.** Gas permeability coefficient of cracked, healed and un-cracked control discs.

The self-healing durability was further studied, using the cracked discs gas permeability performance. There were two set of discs for each type of samples and out of these two, one set of three discs was disposed after initial permeability tests, as methanol may negatively impact the autogenous self-healing mechanisms. The coefficient of gas permeability of discs before and after healing is shown in figure 17. The gas permeability performance before and after healing was showing a similar trend, as was observed in the absorption test results. However, MgO addition in the samples has resulted in a

considerable reduction in the permeability coefficient compared to control. While MgO-PC mixes after self-healing show reduction in the permeability coefficient almost close to control-uncracked samples (only about ~2 times), it was about ~8 times for crack control discs after healing. There was a minor decrease in the coefficient for control samples, which indicates natural autogenous self-healing. The addition of MgO has resulted in further improvement in autogenous self-healing, which eventually causes considerable improvement in the gas permeability results.

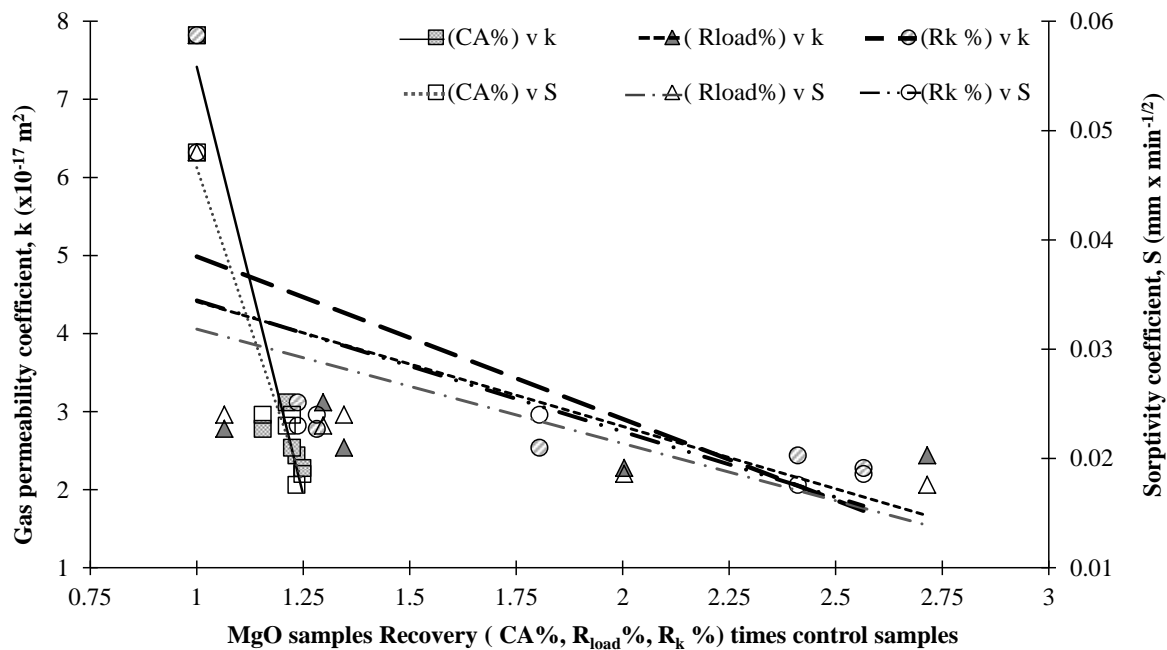


**Figure 18.** Sorptivity and gas permeability coefficients correlation with all samples' self-healing recovery compared to control samples (CA %: crack area closure over time,  $R_{load}$  %: first cracking load lapsing recovery % and  $R_k$  %: stiffness improvement %).

The correlation between overall self-healing parameters is shown in figure 18. All three self-healing recovery parameters (CA %,  $R_{load}$  % and  $R_k$  %) were proportionate with control samples' results and plotted against the corresponding gas permeability and sorptivity coefficient. There was a similar correlation between gas permeability and sorptivity coefficient in most cases. Both permeability and sorptivity coefficient show a decreasing trend, with the increase in all three recoveries. Therefore efficient crack sealing resulted not only in a higher load recovery and stiffness improving trend, but also showed improvement in durability parameters i.e. a decreases in gas permeability and sorptivity coefficients. However, few discrepancies out of the trend were spotted, due to the result of M92-12 and N50 samples wider cracking, initial higher stiffness and first cracking load. Therefore excessive proportions of MgO in PC were not always showed better performances in terms of overall self-healing improvement. This progressive correlation has directed us back to the previous section's arguments regarding the optimum mix proportions for optimum self-healing performances in all aspects. . Therefore, based on the MgO reactivity and mix proportions, the desirable self-healing performance could be designed. The desirable MgO-cement mixes could be designed either based rapid crack sealing and durability improvement, or the ultimate optimum self-healing performance including strength improvement.

#### 4. Conclusions

This study has investigated the autogenous self-healing of drying shrinkage cracks of PC with two reactive grades of expansive MgO (M92-200 and N50). The addition of both reactive grades of MgO

improved the autogenous drying shrinkage crack self-healing capacity of cement. Out of both grades of MgO, highly reactive N50 mixes show higher expansion compared to moderately reactive M92-200 mixes. All samples cured in water showed expansions, and all samples left in the ambient condition expands over time. Expansion and shrinkage of mixes were increasing with the higher reactive grade and proportions MgO. The drying shrinkage was causing cracks in the restrained end prism samples. Average crack widths prior to healing were almost proportional to their drying shrinkage properties, as the greater the shrinkage, the larger the crack width. Overall MgO samples resulted in a crack area reduction of about 74-99% between 14 to 56 days, which is much higher compared to the control samples' 43-79% reduction in the same period. The effective crack sealing has caused considerable durability improvement in the samples, as found in the sorptivity and gas permeability results. Samples were found to have expanded while cured in an immersed condition for self-healing. This expansion allows the crack tips to come closer, which accelerates the self-healing mechanisms. Samples contained higher proportions of expansive MgO showed higher expansive properties during healing, thus resulting in wider cracks being healed more efficiently. Overall self-healing due to both types of MgO addition in PC have increased the crack sealing and strength recovery (load recovery and stiffness improvement) and improved the durability as evident in the gas permeability and sorptivity coefficients. However, there is a threshold in the amount of expansive MgO, which triggers the optimum self-healing performance, considering the strength improvement and durability. These optimum results were found in the 8% MgO (M92-200) followed by 4-8% (N50) samples. In the microstructural investigations, MgO was found to have influence in the formation of brucite and different phases of hydromagnesites, hydrotelcrite and even magnesian calcite. Higher proportions and reactivity of MgO have resulted in the formation of a more stable state of Mg-hydro carbonates. These hydration products cause additional expansion, contributing to autogenous self-healing. Further research is needed to explain complete self-healing kinetics and to explore the possibilities of other expansive minerals for further optimising the self-healing performances for application in concrete industries.

### **Acknowledgements**

The support of the Islamic Development Bank (IDB) scholarship, collaborating with the Cambridge Commonwealth, European and International Trust (CCEIT) for the first author's PhD research, is highly appreciated. The authors also thank Wai Yuk Lau for his assistance and suggestions in the shrinkage measuring experiments.

### **References**

- [1] J. Bisschop and J. G. . van Mier, "How to study drying shrinkage microcracking in cement-based materials using optical and scanning electron microscopy?," *Cem. Concr. Res.*, vol. 32, no. 2, pp. 279–287, Feb. 2002.
- [2] C.-L. Hwang and J. F. Young, "Drying shrinkage of portland cement pastes I. Microcracking during drying," *Cem. Concr. Res.*, vol. 14, no. 4, pp. 585–594, Jul. 1984.
- [3] J. Bisschop and J. G. M. van Mier, "Effect of aggregates on drying shrinkage microcracking in cement-based composites," *Mater. Struct.*, vol. 35, no. 8, pp. 453–461, Sep. 2002.
- [4] T. Shiotani, J. Bisschop, and J. G. . Van Mier, "Temporal and spatial development of drying shrinkage cracking in cement-based materials," *Eng. Fract. Mech.*, vol. 70, no. 12, pp. 1509–1525, Aug. 2003.

- [5] P. Goltermann, "Mechanical Predictions of Concrete Deterioration; Part 2: Classification of Crack Patterns," *Mater. J.*, vol. 92, no. 1, pp. 58–63, Jan. 1995.
- [6] M. Rooij, K. van Tittelboom, N. Belie, and E. Schlangen, Eds., *Self-Healing Phenomena in Cement-Based Materials: State-of-the-Art Report of RILEM Technical Committee 221-SHC: Self-Healing Phenomena in Cement-Based Materials*. Springer, 2013.
- [7] K. Lauer and F. Slate, "Autogenous Healing of Cement Paste," *ACI J. Proc.*, vol. 52, no. 6, pp. 1083–1098, 1956.
- [8] R. K. Dhir, C. M. Sangha, and J. G. L. Munday, "Strength and Deformation Properties of Autogenously Healed Mortars," *J. Am. Concr. Inst.*, vol. 70, no. 70, pp. 231–236, 1973.
- [9] E. F. Wagner, "Autogenous Healing of Cracks in Cement-Mortar Linings for Gray-Iron and Ductile-Iron Water Pipe," *Am. Water Work. Assoc.*, vol. 66, no. 6, pp. 358–360, 1974.
- [10] C. Edvardsen, "Water permeability and autogenous healing of cracks in concrete," *ACI Mater. J.*, 1999.
- [11] W. Ramm and M. Biscop, "Autogenous healing and reinforcement corrosion of water-penetrated separation cracks in reinforced concrete," *Nucl. Eng. Des.*, vol. 179, no. 2, pp. 191–200, Feb. 1998.
- [12] H.-W. Reinhardt and M. Jooss, "Permeability and self-healing of cracked concrete as a function of temperature and crack width," *Cem. Concr. Res.*, vol. 33, no. 7, pp. 981–985, Jul. 2003.
- [13] N. ter Heide and E. Schlangen, "Self-healing of early age cracks in concrete," in *First international conference on self healing materials*, 2007.
- [14] H. Mihashi and T. Nishiwaki, "Development of Engineered Self-Healing and Self-Repairing Concrete-State-of-the-Art Report," *J. Adv. Concr. Technol.*, vol. 10, no. 5, pp. 170–184, 2012.
- [15] Y. Yang, E.-H. Yang, and V. C. Li, "Autogenous healing of engineered cementitious composites at early age," *Cem. Concr. Res.*, vol. 41, no. 2, pp. 176–183, Feb. 2011.
- [16] D. Homma, H. Mihashi, and T. Nishiwaki, "Self-Healing Capability of Fibre Reinforced Cementitious Composites," *J. Adv. Concr. Technol.*, vol. 7, no. 2, pp. 217–228, 2009.
- [17] D. J. Hannant and J. G. Keer, "Autogenous healing of thin cement based sheets," *Cem. Concr. Res.*, vol. 13, no. c, pp. 357–365, 1983.
- [18] T. Qureshi and A. Al-Tabbaa, "The effect of magnesia on the self-healing performance of Portland cement with increased curing time," in *1st International Conference on Ageing of Materials & Structures*, 2014, pp. 635–642.
- [19] T.-H. Ahn and T. Kishi, "Crack Self-healing Behavior of Cementitious Composites Incorporating Various Mineral Admixtures," *J. Adv. Concr. Technol.*, vol. 8, no. 2, pp. 171–186, 2010.
- [20] K. Sisomphon, O. Copuroglu, and E. a. B. Koenders, "Self-healing of surface cracks in mortars with expansive additive and crystalline additive," *Cem. Concr. Compos.*, vol. 34, no. 4, pp. 566–574, Apr. 2012.

- [21] Z. Jiang, W. Li, and Z. Yuan, "Influence of mineral additives and environmental conditions on the self-healing capabilities of cementitious materials," *Cem. Concr. Compos.*, vol. 57, pp. 116–127, Mar. 2015.
- [22] Y.-S. Lee and J.-S. Ryou, "Self healing behavior for crack closing of expansive agent via granulation/film coating method," *Constr. Build. Mater.*, vol. 71, pp. 188–193, Nov. 2014.
- [23] E. Herbert and V. Li, "Self-Healing of Microcracks in Engineered Cementitious Composites (ECC) Under a Natural Environment," *Materials (Basel)*, vol. 6, no. 7, pp. 2831–2845, Jul. 2013.
- [24] B. Suryanto, S. A. Wilson, W. J. McCarter, and T. M. Chrisp, "Self-healing performance of engineered cementitious composites under natural environmental exposure," *Adv. Cem. Res.*, pp. 1–10, Dec. 2015.
- [25] T. Murakami, T. H. Ahn, T. Hashimoto, N. Ogura, and T. Kishi, "A study on the new water leak repair method for subway tunnels using crack self-healing repair materials," in *Fifth International Conference of Self-healing Materials*, 2015.
- [26] H. Jonkers and R. Mors, "Full scale application of bacteria-based self-healing concrete for repair purposes," ... *Retrofit. ICCRRR-3, 3-5 ...*, 2012.
- [27] T. Qureshi and A. Al-Tabbaa, "Influence of Expansive minerals on the Self-healing of Cement Paste and Mortar Systems," in *Fifth International Conference of Self-healing Materials*, 2015.
- [28] F. Jin and A. Al-Tabbaa, "Characterisation of different commercial reactive magnesia," *Adv. Cem. Res.*, vol. 26, no. 2, pp. 101–113, 2014.
- [29] B. EN, "197-1: 2011. British Standard. Part I: Composition, Specifications and Conformity Criteria for Common Cements," 2011.
- [30] F. Jin and A. Al-Tabbaa, "Characterisation of different commercial reactive magnesia," *Adv. Cem. Res.*, 2013.
- [31] M. Shand, *The chemistry and technology of magnesia*. 2006.
- [32] C. K. Chau and Z. Li, "Accelerated reactivity assessment of light burnt magnesium oxide," *J. Am. Ceram. Soc.*, vol. 91, no. 23712, pp. 1640–1645, 2008.
- [33] BSEN12617-4:, "Products and systems for the protection and repair of concrete structures. Test methods. Determination of shrinkage and expansion," 2002.
- [34] BS EN:196-1, "Methods of testing cement. Determination of strength," 2005. [Online]. Available: <http://shop.bsigroup.com/ProductDetail/?pid=000000000019983596>. [Accessed: 16-May-2015].
- [35] A. Kanellopoulos, T. S. Qureshi, and A. Al-Tabbaa, "Glass encapsulated minerals for self-healing in cement based composites," *Constr. Build. Mater.*, vol. 98, pp. 780–791, Nov. 2015.
- [36] T. S. Qureshi, A. Kanellopoulos, and A. Al-Tabbaa, "Enhancing Autogenous Self-healing of Portland Cement through Partial Substitution with Expansive Minerals, (submitted manuscript)," *Cem. Concr. Res.*, Oct. 2015.



- [37] J. Kropp, "RILEM Technical committees RILEM TC 116-PCD : Permeability of Concrete as a Criterion of its Durability Recommendations, test for gas permeability of concrete a preconditioning of concrete test specimens for the measurement of gas permeability and capilar," *Mater. Struct.*, vol. 32, no. April, pp. 174–179, 1999.
- [38] C. Hall and T. K.-M. Tse, "Water movement in porous building materials—VII. The sorptivity of mortars," *Build. Environ.*, vol. 21, no. 2, pp. 113–118, 1986.
- [39] A. M. Alshamsi and H. D. a Imran, "Development of a permeability apparatus for concrete and mortar," *Cem. Concr. Res.*, vol. 32, no. July 2000, pp. 923–929, 2002.
- [40] Z. Yang, J. Hollar, X. He, and X. Shi, "A self-healing cementitious composite using oil core/silica gel shell microcapsules," *Cem. Concr. Compos.*, vol. 33, no. 4, pp. 506–512, Apr. 2011.
- [41] L. Mo, M. Deng, M. Tang, and A. Al-Tabbaa, "MgO expansive cement and concrete in China: Past, present and future," *Cem. Concr. Res.*, vol. 57, pp. 1–12, Mar. 2014.
- [42] L. Mo, M. Deng, and M. Tang, "Effects of calcination condition on expansion property of MgO-type expansive agent used in cement-based materials," *Cem. Concr. Res.*, vol. 40, no. 3, pp. 437–446, Mar. 2010.
- [43] M. Trezza and A. Lavat, "Analysis of the system  $3\text{CaO} \cdot \text{Al}_2\text{O}_3\text{-CaSO}_4 \cdot 2\text{H}_2\text{O-CaCO}_3\text{-H}_2\text{O}$  by FT-IR spectroscopy," *Cem. Concr. Res.*, 2001.
- [44] P. Yu and R. Kirkpatrick, "Structure of calcium silicate hydrate (C-S-H): Near-, Mid-, and Far-infrared spectroscopy," *J. Am. Ceram. Soc.*, vol. 82, no. 3, pp. 742–748, 1999.
- [45] L. Fernandez, C. Alonso, C. Andrade, and A. Hidalgo, "The role of magnesium during the hydration of C3S and C-S-H formation. Scanning electron microscopy and mid-infrared studies," *Advances in Cement Research*, vol. 17, no. 1. pp. 9–21, 2005.
- [46] R. Ylmén, U. Jäglid, B. M. Steenari, and I. Panas, "Early hydration and setting of Portland cement monitored by IR, SEM and Vicat techniques," *Cem. Concr. Res.*, vol. 39, no. 5, pp. 433–439, 2009.
- [47] A. A. Reddy, A. Goel, D. U. Tulyaganov, S. Kapoor, K. Pradeesh, M. J. Pascual, and J. M. F. Ferreira, "Study of calcium–magnesium–aluminum–silicate (CMAS) glass and glass-ceramic sealant for solid oxide fuel cells," *J. Power Sources*, vol. 231, pp. 203–212, Jun. 2013.
- [48] J. I. Escalante-García, A. F. Fuentes, A. Gorokhovskiy, P. E. Fraire-Luna, and G. Mendoza-Suarez, "Hydration Products and Reactivity of Blast-Furnace Slag Activated by Various Alkalis," *J. Am. Ceram. Soc.*, vol. 86, no. 12, pp. 2148–2153, Dec. 2003.
- [49] S. Song and H. Jennings, "Pore solution chemistry of alkali-activated ground granulated blast-furnace slag," *Cem. Concr. Res.*, vol. 29, no. 2, pp. 159–170, 1999.
- [50] C. Unluer and A. Al-Tabbaa, "Impact of hydrated magnesium carbonate additives on the carbonation of reactive MgO cements," *Cem. Concr. Res.*, vol. 54, pp. 87–97, Dec. 2013.
- [51] S. Teir, S. Eloneva, C. J. Fogelholm, and R. Zevenhoven, "Fixation of carbon dioxide by producing hydromagnesite from serpentinite," *Appl. Energy*, vol. 86, no. 2, pp. 214–218, 2009.

- [52] J. I. Escalante-Garcia and J. H. Sharp, "Variation in the Composition of C-S-H Gel in Portland Cement Pastes Cured at Various Temperatures," *J. Am. Ceram. Soc.*, vol. 82, no. 11, pp. 3237–3241, Dec. 2004.